Sensitive dependence of trajectories on tracer seeding positions - coherent structures in German Bight backward drift simulations

Ulrich Callies[1]

[1]Institute of Coastal Research, Helmholtz-Zentrum Geesthacht, Max-Planck-Str. 1, 21502 Geesthacht, Germany

Correspondence: Ulrich Callies (ulrich.callies@hzg.de)

Abstract. Backward drift simulations can aid the interpretation of in situ monitoring data. In some cases, however, trajectories are very sensitive to even small changes of the tracer release position. A corresponding spread of backward simulations implies attraction in the forward passage of time and hence uncertainty about the probed water body's origin. This study examines surface drift simulations in the German Bight (North Sea). Lines across which drift behaviour changes non-smoothly are obtained as ridges in the fields of the finite-time Lyapunov exponent (FTLE), a parameter used in dynamical systems theory to identify Lagrangian coherent structures (LCS). Results closely resemble those obtained considering two-particle relative dispersion. It is argued that simulated FTLE fields might be used in support of the interpretation of monitoring data, indicating also vagueness of drift simulations being used.

1 Introduction

In the German Bight area (North Sea) a comprehensive monitoring network is operated, including the Marine Environmental Monitoring Network in the North Sea (MARNET), the Coastal Observing System for the North and Arctic Seas (COSYNA) and other stations. Details on the type of data being collected can be found in Baschek et al. (2017). Stanev et al. (2016) discuss issues related to modelling and data assimilation with spatiotemporal optimal interpolation. Multivariate statistical methods can also be used for optimizing the design of observational arrays (e.g. Chen et al., 2016; Kim and Hwang, 2020). When it comes to the analysis of specific data, however, a merely statistical description of spatial connectivity falls short of what can be achieved if hydrodynamic current fields from either models or remote sensing are available.

Backward tracer trajectories seeded at monitoring stations provide insight into the background of water bodies that were probed (e.g. d'Ovidio et al., 2015; Lucas et al., 2016; Teeling et al., 2012, supplement, movie S1), helping distinguish between temporal and spatial variability, i.e. local changes and advection from somewhere else. Backtracking water bodies from hypothetical monitoring stations in the vicinity of Helgoland, Callies et al. (2011, their Fig. 3) provide an example of how quasi-chaotic mixing in two-dimensional barotropic simulations transforms initially regular into quite contorted structures. Also in nature, forward trajectories of drifters released pairwise may separate quite fast (e.g. Callies et al., 2019; Meyerjürgens

et al., 2020). Therefore, a key question is how reliable backward drift analyses can be and how the numerical analysis of a water body's recent history should be designed. In addition to well known random dispersion there exist also flow patterns that affect separation of simulated backward trajectories more systematically (Haller, 2015). The present study focuses on this latter aspect, i.e. coherent structures shaping separation of simulated backward trajectories.

A statistical measure of particle spreading is relative dispersion, the mean square particle distance, as function of time. LaCasce (2008) reviews how this parameter relates to the energy spectrum of a turbulent flow. Relative dispersion is called local when particle separation is dominated by small eddies with a typical scale that compares with particle separation. By contrast, it is termed non-local if particle separation is dominated by eddies much larger than particle separation. In the latter case, characterized by a steep energy spectrum, particle separation is expected to grow exponentially. Such very high sensitivity to initial particle positions implies what in dynamical systems theory is called chaotic advection (Wiggins, 2005).

Dynamical systems theory aims at a description of the kinematics of turbulent mixing. The approach is based on flow maps that describe particle advection over some time interval, according to Haller (2015) "*thereby mimicking experimental flow visualization by tracers*". This technique has widely been applied for analysing the microstructure of chaotic mixing processes in two dimensions (e.g. Pierrehumbert and Yang, 1993), describing how chaotic advection may transform initially small disks of fluid into complex filamentary structures. Trying to improve the sometimes vague definitions of such structures, Haller and Yuan (2000) introduced the framework of Lagrangian coherent structures (LCS). Their method seeks to identify material lines that function as only weekly permeable barriers for water body transport, attracting or repelling neighboured trajectories. Peacock and Haller (2013) provide a nice overview of the topic.

Attracting LCSs, in dynamical systems theory also called unstable because of a fast stretching of particles along them (according to Harrison and Glatzmaier (2010) an unfortunate historical definition), have been used for optimizing drifter deployments in field studies. Poje et al. (2002) proposed drifter deployment into attracting LCSs to ensure fast dispersal based on near-exponential material stretching, which lets drifters explore regions of high kinetic energy. Molcard et al. (2006) used this approach for assimilating drifter velocities into an ocean general circulation model. Different from these studies, Shadden et al. (2009) focus on repelling LCSs. Seeding drifters in a less localized way, Shadden et al. try to make drifters stay as long as possible in a specific region delineated by transport barriers. They exemplify that a LCS's robustness might enable extrapolation of its separatrix function even beyond the time horizon of detailed operational hydrodynamic predictions (e.g. three days). Combining SeaWiFS ocean-colour data with altimetry-derived surface currents in the Brazil-Malvinas confluence zone, d'Ovidio et al. (2010) found that stirring by mesoscale currents can play an important role in structuring phytoplankton communities and even create what they call fluid dynamical niches, sharply delimited by LCSs. Hernández-Carrasco et al. (2018) study this topic at the submesoscale, using currents observed with High-Frequency Radar (HFR) in coastal waters. According to Scales et al. (2018) attracting LCSs can also be targeted by fisheries, led by lines of drifting foam or debris.

Conducting backward simulations, the present study proposes the use of LCSs as indicators of a possibly sensitive dependence of measurements on where and when exactly they were taken. The analysis is based on offline drift simulations using German Bight surface layer currents obtained from archived output of the operational 3D baroclinic model BSHcmod, run operationally by the German Federal Maritime and Hydrographic Agency (BSH). The study aims for an assessment of the

situations at specific times of interest rather than for a generic characterization or classification of given locations. Highly variable transport paths in the German Bight area for the most part arise from residual currents being driven by changing wind conditions (Schrum, 1997; Callies et al., 2017a). Establishing a simple interrelationship between winds and overall finite-time transports is hardly possible, tracer trajectories aggregate the effects of possibly very different winds. Detailed numerical simulations, however, properly integrate such variable hydrodynamic transports during a specific observation period.

Hadjighasem et al. (2017) compare twelve candidate approaches that could be used for the identification of LCSs. Among those, calculation of finite-time Lyapunov exponents (FTLE) is one of the most common methods. It is closely related to the finite-scale Lyapunov exponent (FSLE), originally introduced by Aurell et al. (1996, 1997) and used in experiments for diagnosing scale dependent separation rates between drifter pairs (LaCasce and Ohlmann, 2003; Sansón et al., 2017). Karrasch and Haller (2013), however, report some limitations for FSLE in LCS detection, suggesting that an approach based on FTLE distributions may be more reliable. The FTLE fields are independent of an observer's reference frame (Haller, 2015), representing the rate at which neighbouring tracers separate according to the largest eigenvalue of the so-called Cauchy-Green strain tensor.

Building on work by Haller (2001), Shadden et al. (2005) define LCS in terms of ridges in the FTLE field. In two dimensions, the LCSs are material lines transported with the flow and, in good approximation, acting as transport barriers. Haller (2011), discussing counterexamples in which substantial material flows cross a FTLE ridge occurred, developed a more sophisticated variational approach, Farazmand and Haller (2012) presented a corresponding numerical algorithm for two-dimensional applications. Recently Tian et al. (2019) applied a variational method to identify the outer bounds of the Kuroshio current system. Here, the analysis will adhere to conventional FTLE fields.

The paper is organized as follows: Section 2 first describes the study area and how Lagrangian drift simulations were performed based on pre-calculated hydrodynamic surface current fields. It follows a short compilation of the definitions of the FTLE, Lagrangian divergence and statistical measures of dispersion. Presenting a couple of structures that emerged under different wind conditions, Section 3 then tries to give an overview of the type of LCSs that can be found in the German Bight area. Example trajectories substantiate the relevance of FTLE ridges as material separatrices. A general discussion and a short summary conclude the paper.

2 Material and methods

2.1 Study area

The North Sea is a semi-enclosed shelf sea that connects to the north-eastern Atlantic at its northern boundary and through the English Channel at its southwest (Sündermann and Pohlmann, 2011). Strong tidal forcing occurs as a co-oscillation triggered by Atlantic tidal waves. This study focusses on the German Bight, the shallow south-eastern part of the North Sea (here: east of 6.5°E and south of 56°N) with water depths of mainly 20-50 m (see Fig. 1), adjoining the Dutch, the German and the Danish coasts (Becker et al., 1992). In the German Bight, a mean cyclonic North Sea circulation corresponds with residual currents from the southwest to the north. Superimposed to this mean circulation, a strong weather driven variability occurs on short time scales (Schrum, 1997; Callies et al., 2017a). A fresh water plume emerging from the Elbe River and, to a minor extent,

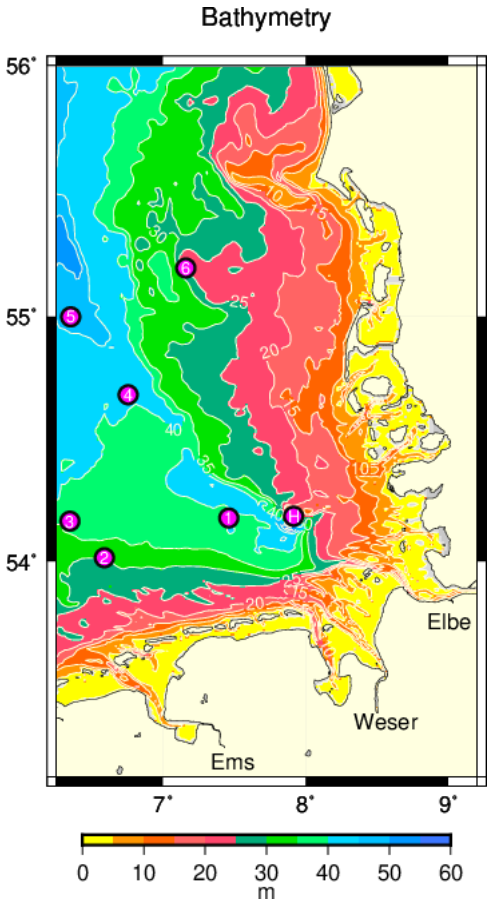

Figure 1. German Bight bathymetry. Magenta coloured circles indicate locations of six stations of the MARNET monitoring network (labels 1-6) and of the island of Helgoland (label H).

also the Weser and the Ems rivers can be observed as a permanent feature. Transient eddies and meanders depend on bottom topography, baroclinic instabilities and wind effects.

The most important topographic feature is the old Elbe Glacial Valley, opening from today's Elbe estuary towards the northwest into the open North Sea (see Fig. 1). Becker et al. (1992) summarize different types of fronts (river plume, thermal and upwelling fronts) that occur in the German Bight. Frontal structures depend on season but vary also on a short term basis (Budéus, 1989; Schrum, 1997). In the warm season, strong stratification occurs at water depths greater than approximately 30 m, mainly in the Elbe Glacial Valley. A baroclinic tidal mixing front (James, 1984; Holt and Umlauf, 2008) separates this region from the well-mixed more shallow coastal water, where stratification is prevented by strong tidal mixing (Krause et al., 1986).

2.2 Hydrodynamic fields

Surface layer currents used for offline drift simulations (see Section 2.3) as well as temperature fields were taken from archived BSHcmod model output. BSHcmod is a three-dimensional baroclinic circulation model, formulated using geographical coordinates and a flexible vertical resolution that allows for weakly inclined coordinate surfaces (Dick et al., 2008) of up to 36 layers. The model is run operationally by the Federal Maritime and Hydrographic Agency (BSH) since many years, providing the basis for different oceanographic services including search-and-rescue applications. It covers both the North Sea and the Baltic Sea and is two-way nested with approximately 900 m resolution in the German Bight area (Fig. 1) and approximately 5 km in the open North Sea (Dick et al., 2001). The domain of the present analysis roughly agrees with the region of 900 m resolution in German North Sea coastal waters.

In BSHcmod, advection and diffusion are calculated using a flux-corrected transport scheme. The hydrostatic and the Boussinesq approximations are applied. The Smagorinsky scheme (Smagorinsky, 1963) is used for the parameterization of horizontal viscosity. For an inclusion of wind stress, the parametrization by Smith and Banke (1975) is used. Stokes drift remains disregarded in the operational model output. The model's atmospheric forcing is provided by the regional model COSMO-EU (Consortium for Small-Scale Modelling; Schulz and Schättler (2014)), run by the German Meteorological Service (Deutscher Wetterdienst – DWD). The Swedish Meteorological and Hydrological Institute (SMHI) and the Federal Institute of Hydrology (BfG) provide runoff data for all major rivers that flow into the North Sea.

In the process of archiving, BSHcmod hydrodynamic fields with originally higher vertical resolution were re-gridded. Conserving transport rates, this was done in such a way that the archived surface currents used in this study are representative for the uppermost 5 metres of the water column. With drift simulations based on these currents plus a leeway of 0.6 % of wind in 10 m height, Callies et al. (2017b, 2019) reproduced observed drifter trajectories reasonably well.

2.3 Lagrangian drift simulations

Offline drift simulations were performed using the Lagrangian transport program PELETS-2D (Callies et al., 2011), based on BSHcmod surface layer currents, archived on a 15 min basis. Originally, the PELETS toolbox developed at Helmholtz-Zentrum Geesthacht was designed for its use with hydrodynamic currents on unstructured triangular grids. Current fields provided on a regular grid (like those from BSHcmod) must be preprocessed, splitting each rectangular grid cell into two triangles, a transformation of grid topology that does not affect the information content of hydrodynamic fields.

All simulations in this study were produced using the fourth-order Cash Karp method (Press et al., 1992) that belongs to the Runge Kutta family of solvers. A simple Euler forward scheme, however, used in other PELETS applications (e.g. Callies et al., 2011, 2017b, 2019) gave very similar results. The maximum time step is set to 15 min. Velocities are updated earlier if a tracer particle moves to another triangular grid cell.

2.4 Finite-time Lyapunov exponents (FTLE)

Definition of the FTLE is based on a consideration of Lagrangian flow motions. A flow map Φ maps particle locations $\boldsymbol{x}_0$, where particles were seeded at time t_0, onto their destinations $\boldsymbol{x}$ at later time $t = t_0 + \tau$:

$$\Phi_{t_0}^{\tau}(\boldsymbol{x_0}) = \boldsymbol{x}(t_0 + \tau; t_0, \boldsymbol{x}_0) \; . \tag{1}$$

The following deformation gradient describes material deformation,

$$\nabla \Phi_{t_0}^{\tau}(\boldsymbol{x_0}) = \begin{pmatrix} \frac{\partial x}{\partial x_0} & \frac{\partial x}{\partial y_0} \\ \frac{\partial y}{\partial x_0} & \frac{\partial y}{\partial y_0} \end{pmatrix} \; , \tag{2}$$

where $\boldsymbol{x} = (x, y)$. The deformation's Jacobian provides the ratio of the area A of a deformed quadrangle to the area A_0 of an infinitesimal square it has its origin in. In case of a finite size initial square and a non-linear flow, this ratio refers to a quadrangle that approximates the emerging distorted patch. Similarly, a linear map sends an initially small circle to an ellipse. The lengths of the image area's semi-axes are given by the deformation gradient's two singular values μ_1, μ_2, whose product equals the Jacobian determinant:

$$\frac{A}{A_0} = \det\left(\nabla \Phi_{t_0}^{\tau}\right) = \mu_1 \mu_2 \; . \tag{3}$$

From the above deformation gradient, one obtains the following Cauchy-Green strain or deformation tensor (e.g. Shadden et al., 2005; Haller, 2015):

$$C(\tau; t_0, \boldsymbol{x}_0) = \left[\nabla \Phi_{t_0}^{\tau}(\boldsymbol{x}_0)\right]^T \nabla \Phi_{t_0}^{\tau}(\boldsymbol{x}_0) \; . \tag{4}$$

This two-dimensional, symmetric and positive-definite tensor has two eigenvalues $\lambda_1 = \mu_1^2$ and $\lambda_2 = \mu_2^2$. Definition of the finite-time Lyapunov exponent (FTLE) is based on the tensor's larger eigenvalue λ_1:

$$\mathrm{FTLE}\,(\tau; t_0, \boldsymbol{x}_0) = \frac{1}{\mid \tau \mid} \log \sqrt{\lambda_1} = \frac{1}{\mid \tau \mid} \log(\mu_1) \; . \tag{5}$$

The absolute value of integration time τ is used because integration of particle drift can be conducted either forward or backward in time. The geometric interpretation of the FTLE refers to the maximum separation rate of neighbouring particles (Haller, 2015).

To compute FTLE fields numerically, a regular Cartesian grid of tracers was released, initial locations with 1 km resolution covering the German Bight area east of 6.5°E and south of 56°N (165 vortices in the longitudinal and 310 vortices in the latitudinal direction). The corresponding 51150 trajectories were integrated 250 hours back in time (τ = -250 h). To avoid the

computational burden of four close-by auxiliary trajectories, finite-differencing (Eq. 2) was performed based on neighbouring trajectories already seeded on the regular FTLE grid.

In view of the limited vertical resolution of archived BSHcmod currents, values of the deformation gradient (Eq. (2)) were tagged as missing each time at least one of the four tracer trajectories needed for its discrete calculation encountered a water depth of less than 5 m sometime in the course of its integration. Resulting gaps in the fields of FTLE and related quantities change with variable atmospheric forcing. As BSHcmod covers the whole North Sea, no specific treatment is needed for particles that cross the open boundaries of the FTLE grid.

2.5 Distinction between divergence and stretch

An incompressible two-dimensional flow field preserves the area of a Lagrangian patch during arbitrary deformations. Here, however, two-dimensional surface currents being used were extracted from three-dimensional hydrodynamic fields that allow for vertical exchange of water masses. Huntley et al. (2015) developed a concept that splits FTLE values into contributions that come from area-preserving stretching and deformation on the one hand and area changes on the other. Given the singular values $\mu_1 \geq \mu_2$ of the deformation gradient $\nabla \Phi_{t_0}^{\tau}(\boldsymbol{x_0})$, Huntley et al. (2015) introduce the following stretch rate Σ:

$$\Sigma = \frac{1}{\mid \tau \mid} \log\left(\frac{\mu_1}{\mu_2}\right) . \tag{6}$$

In addition, they introduce the following dilation rate Δ that describes the transformation of a Lagrangian patch's initial area A_0 to an area A after integration time τ,

$$\Delta = \frac{1}{\mid \tau \mid} \log\left(\frac{A}{A_0}\right) = \frac{1}{\mid \tau \mid} \log\left(\mu_1 \mu_2\right) , \tag{7}$$

where Eq. (3) has been used. From Eq. (5) it follows that the separation rate represented by the FTLE can be decomposed in terms of the above two components:

$$\mathrm{FTLE} = \frac{\Delta + \Sigma}{2} . \tag{8}$$

Dilation rate Δ can be shown to equal the average Eulerian horizontal divergences experienced by a fluid parcel along its pathway (Huntley et al., 2015; Duran et al., 2018, supplement). From the material derivative

$$\frac{dA}{dt} = A \nabla \cdot \boldsymbol{v} , \tag{9}$$

it follows that

$$A(t) = A_0 \exp\left(\int_{t_0}^{t_0+\tau} \nabla \cdot \boldsymbol{v}(t', \boldsymbol{x}(t')) dt' \right) . \tag{10}$$

Hernández-Carrasco et al. (2018) refer to the patch area's change rate, derived from past Eulerian divergences, as the Finite-Domain Lagrangian Divergence (FDLD),

$$\mathrm{FDLD} = \frac{1}{\mid \tau \mid} \log\left(\frac{A}{A_0}\right) = \frac{1}{\mid \tau \mid} \int_{t_0}^{t_0+\tau} \nabla_H \cdot \boldsymbol{v}(t', \boldsymbol{x}(t')) dt' . \tag{11}$$

They demonstrate its potential for supporting the interpretation of satellite based observations of surface chlorophyll *a* patches.

Analytically, the FDLD from Eq. (11) equals the dilation rate Δ from Eq. (7). In the present study, however, Eulerian divergences needed for the numerical evaluation of Eq. (11) were computed introducing auxiliary points at a 250 m distance. Velocities at these auxiliary locations were obtained by linear interpolation. As a result of this approach, estimated FDLD fields have slightly higher resolution than Δ fields derived from deformation gradients specified on the basic 1 km FTLE grid.

2.6 Absolute and relative dispersion

Absolute and relative dispersion are statistical measures for analysing Lagrangian data. Generally, absolute dispersion is defined as the second moment of the single particle displacement PDF, i.e. the variance of particle displacements relative to their starting position. This measure must not be confused with cloud variance (LaCasce, 2008). Ensemble averaging could be performed with respect to either different locations or different realizations at some fixed location. Here, following Haller and Yuan (2000), the simpler density of absolute dispersion is considered, describing just a single particle's squared displacement from its release point:

$$a^2(\tau; t_0, \boldsymbol{x}_0) = \mid \boldsymbol{x}(t_0+\tau; t_0, \boldsymbol{x}_0) - \boldsymbol{x}_0) \mid^2 \tag{12}$$

By contrast, relative dispersion describes the mean square separation of particle pairs with nearby initial release points. Relative dispersion at each node of the FTLE grid will be calculated combining the information from four particle pairs,

$$D^2(\tau; t_0, \boldsymbol{x}_0) = \frac{1}{4}\sum_{i=1}^{4} \mid \boldsymbol{x}(t_0+\tau; t_0, \boldsymbol{x}_0) - \boldsymbol{x}(t_0+\tau; t_0, \boldsymbol{x}_0 + \delta\boldsymbol{x}_i) \mid^2 \tag{13}$$

where $\delta\boldsymbol{x}_i$ denotes the distance vector between neighbouring nodes. For a comparison with FTLE and FDLD fields, the logarithm of absolute and relative dispersion is a reasonable choice. Exponential growth of pair separations indicates the presence of Lagrangian chaos dynamical systems theory deals with (Wiggins, 2005).

3 Results

A couple of examples will be given, intended to illustrate the occurrence and time variability of Lagrangian structures in German Bight surface currents. None of these structures are persistent, occurrence and specific details depend on the past evolution of environmental conditions. All figures contain wind roses that summarize wind conditions during the past 250 hours. A video provided in the supplement exemplifies the time evolution of FTLE fields in the course of the year 2016.

3.1 First example

Fig. 2a shows the FTLE field for simulations initialized on 12 June 2015 (13:00 UTC) and extending over 250 hours backward in time. The graph leaves blank all locations from where trajectories reached regions with water depths below 5 m. At the time Fig. 2 refers to, the most prominent feature in the FTLE field is an extended south-north running ridge of high FTLE values.

Further west, a less pronounced parallel second ridge occurs which, however, tends to be split into three or four segments. Other more local and sometimes also weaker filamentary structures can be recognized. Intended to illustrate the physical relevance of the central FTLE-ridge, Fig. 2a includes three groups of four 250 h backward trajectories, initialized in the wider neighbourhood of stations 1, 4 and 6 of the MARNET monitoring network[1]. To facilitate orientation and comparison, locations of the six MARNET stations and the island of Helgoland (station H) will be indicated in all further figures.

The experiment shown refers to a situation with calm conditions during the last three days, weak winds blowing from the north/northeast under the influence of a high pressure system centred further west. Vectors in the top right corner of Fig. 2a show simulated 10 m wind directions near MARNET station 4 during the past 250 hours at ten hourly intervals. Wind speeds are represented by a colour code. The wind vector at the time of the plot is edged in red, those during the last 50 hours are edged in black. Strong winds (> 17m/s) from south/southwest occurred on the second and third of June, i.e. at the end of the 250 hours backward integration period. Another event with enhanced wind speeds (< 10 m/s) from the north/northwest occurred about 4-6 days before the time of the FTLE field being shown. In this period, wind directions changed from roughly southern to northern directions. Both the directional changes and the higher drift speeds at the end of the integration back in time can also be recognized from the example drift trajectories displayed in Fig. 2a.

Two pairs of hypothetical in situ observation points (indicated by small circles, green and blue) were located on either side of the central FTLE ridge near MARNET stations 1 and 6. Trajectory end points are indicated by small diamonds. Simulations show a clear separation of backward trajectories that emerge from different sides of the FTLE ridge. By contrast, trajectories started on the same side of the ridge (having same colour) remain close to each other. The example backward trajectories illustrate how even close by in situ observations may encounter water bodies with a much different history. A complementary experiment considers four trajectories in the vicinity of MARNET station 4, with now all release points being located within the same area of low FTLE values. In this case all trajectories stay close together or even further converge.

[1]Station names: Deutsche Bucht (1), FINO1 (2), Ems (3), Nordseeboje III (4), Nordseeboje II (5), FINO3 (6)

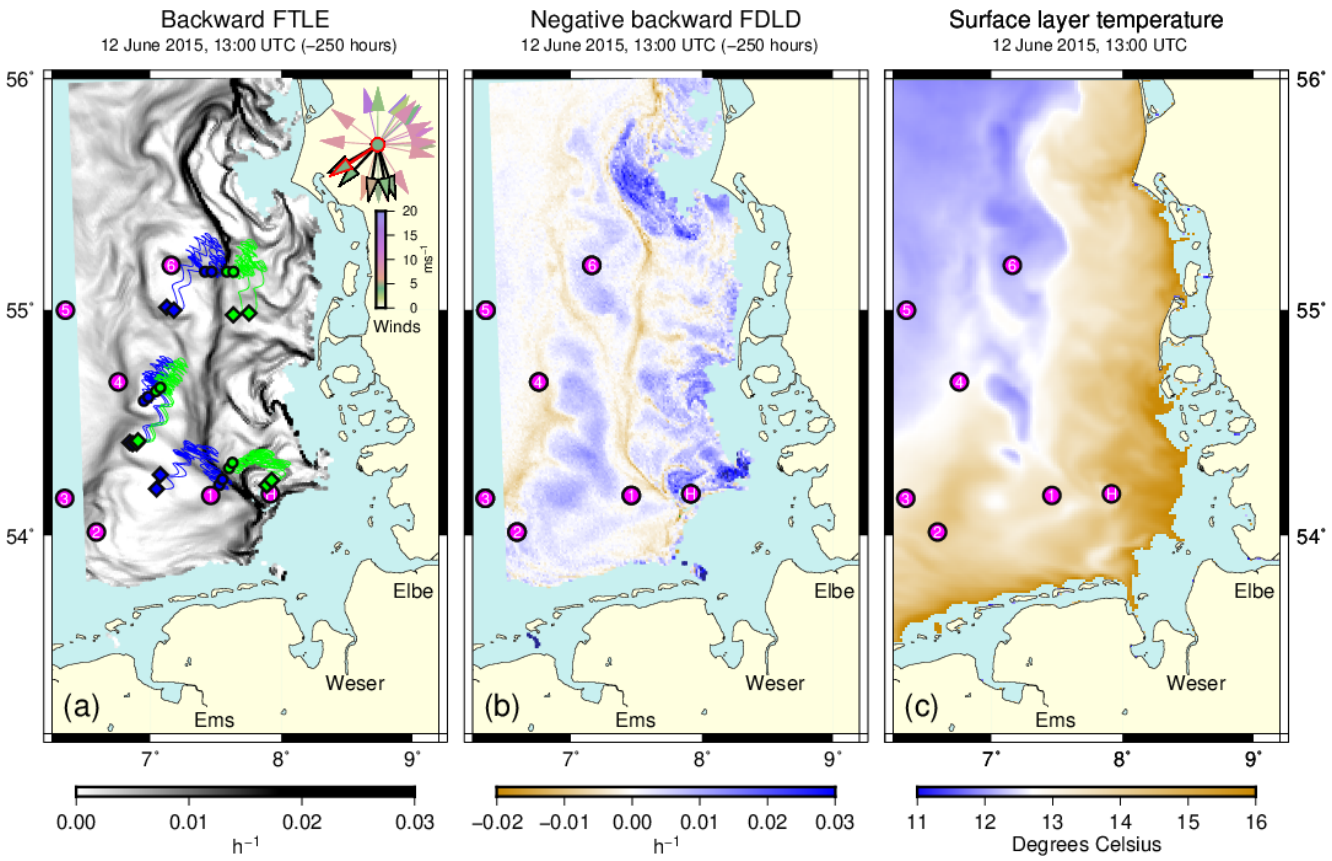

Figure 2. (a) FTLE field analysed for 12 June 2015 (13:00), evaluating Eq. (5) based on trajectories calculated 250 hours backward in time. The scale was chosen to well visualize ridges of large values, negative values of the logarithmic FTLE have been plotted as if they were zero. Locations from where trajectories encountered a water depth of less than 5 m sometime in the course of their integration were disregarded. Example backward trajectories are shown, using different colours (green/blue) for better distinction. Trajectory release points are indicated by circles, small diamonds mark trajectory end points. Labelled circles (magenta) indicate locations of six stations of the MARNET monitoring network (1-6) and of the island of Helgoland (H). Vectors in the top right corner show past wind directions at ten hourly intervals, referring to conditions modelled for the location of MARNET station 4. Different wind speeds are represented by different colours. The wind vector at the time of the plot is edged in red, those during the last 50 hours are edged in black. **(b)** Negative Lagrangian divergences (FDLD) calculated from Eq. (11). Few large positive values, exceeding the range covered by the colour map, are plotted in dark blue. **(c)** Simulated mean temperatures in the uppermost 5 meters. To focus on open sea conditions, temperatures higher than 16°C are not shown.

Separation in backward time means confluence in ordinary forward time. Therefore, the negative backward Lagrangian divergence FDLD (see Eq. (11)) shown in Fig. 2b is to be read in agreement with the usual passage of time. Fig. 2b reveals a striking structural similarity with Fig. 2a. Water parcels located on backward FTLE ridges have predominantly experienced converging surface currents along their pathway during the last 250 hours. Between the ridges, there are wider regions with particles the history of which was dominated by divergent Eulerian currents.

Studying the Agulhas current in the southwest Indian Ocean, van Sebille et al. (2018, their Fig. 3) found structures in fields of sea surface temperature (SST) that agreed with LCSs derived from geostrophic currents. For the present example, Fig. 2c shows a south-north oriented zone of relatively cool surface layer water, located in between narrow bands of higher temperature that tend to coincide with the FTLE ridges (Fig. 2a) and zones of convergence (Fig. 2b). The belt is made up by a couple of patches that bear a structural resemblance to patches of positive divergence in Fig. 2b, suggesting that some features of the temperature distribution in Fig. 2c can indeed be explained in terms of up- and downwelling simulated in the model. Meyerjürgens et al. (2020) found reduced relative dispersion for experimental drifters released in the vicinity of a tidal mixing front, indicating horizontal attraction in this region.

3.2 Second example

Fig. 3b shows a backward FTLE field that is even more clearly structured than the one in Fig. 2a, including also pronounced west-east oriented divides. Note that FTLE ridges in the western part of the domain closely follow the bathymetric feature of the old Elbe Glacial Valley (see Fig. 1). Again, the origins of example tracers, estimated by backward trajectories with close by release points (green/blue) on either side of FTLE ridges, vastly differ. Particularly large differences occur for the most northern and the most southern trajectries.

Similar to the example shown in Fig. 2, calm atmospheric conditions prevailed also for a couple of days preceding the time of Fig. 3b (26 March 2018, 18:00). Very strong easterly winds, however, persisted for a couple of days towards the end of the 250 h backward integration period (roughly 16-18 March). Nearly constant easterly wind directions for the last 50 hours can be distinguished from the wind rose in Fig. 3a, showing the FTLE field eight days earlier. Trajectories of North Sea drifters observed under these rare conditions (due to low temperatures in the UK called the 'Beast from the East') have been discussed by Stanev et al. (2019, see Fig. 3a therein). Some FTLE ridges that emerge according to Fig. 3a are aligned parallel with the easterly winds and seem to correspond with or to transform into sharp FTLE ridges in Fig. 3b under the subsequent much calmer conditions.

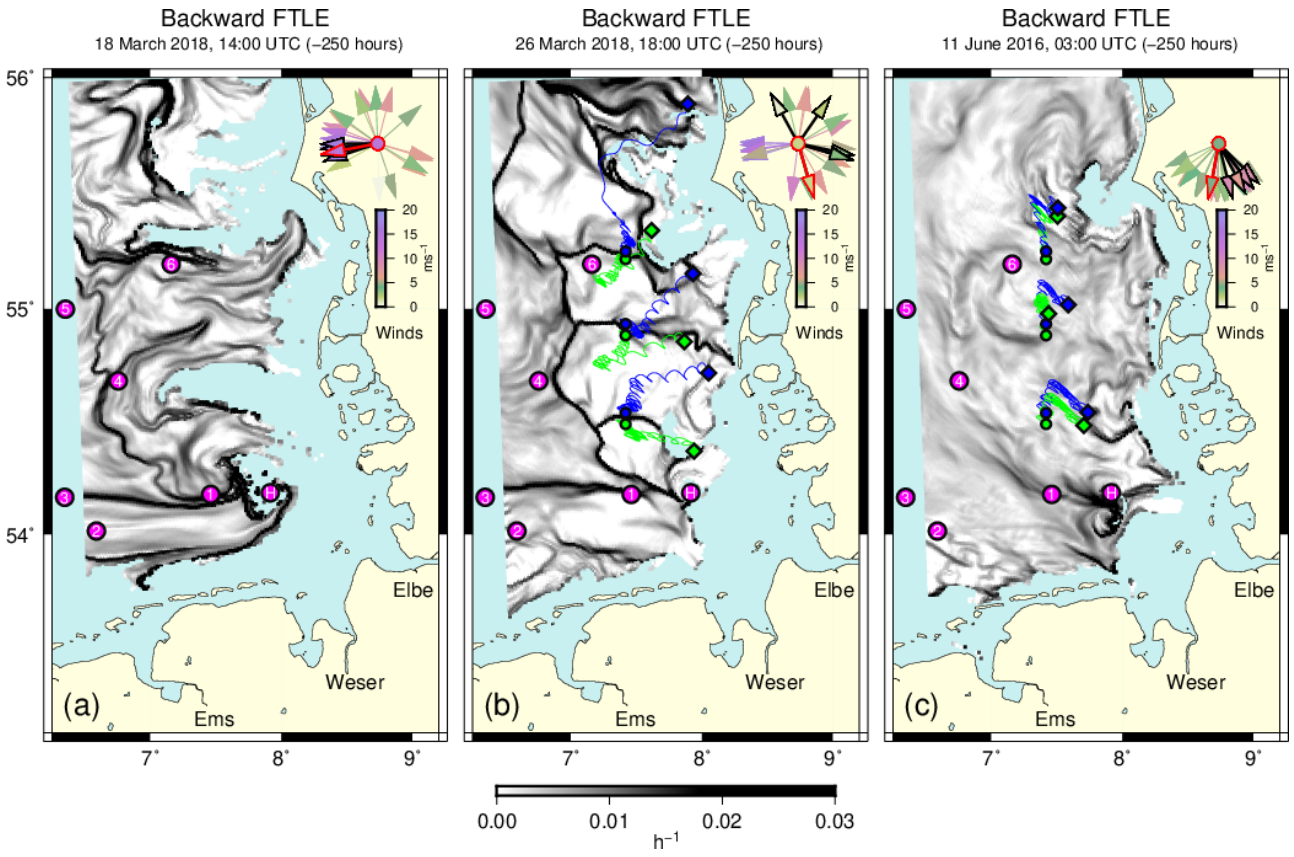

Figure 3. **(a)** Backward FTLE field (250 hours integration) for 18 March 2018 (14:00). Magenta circles indicate locations of MARNET stations (1-6) and of the island of Helgoland (H). **(b)** Backward FTLE field about eight days later (26 March 2018, 18:00). Three pairs of example trajectories (green/blue), started on either side of FTLE ridges, are shown. Trajectory release points are indicated by circles, end points by diamonds. **(c)** Example of a much smoother backward FTLE field on 11 June 2016 (03:00). For the purposes of comparison, backward trajectories were calculated from the same release points used in panel (a). Vectors in the top right corner of each panel show past wind directions (modelled for the location of MARNET station 4) at ten hourly intervals. Different wind speeds are represented by different colours. Wind vectors at the times plots refer to are edged in red, those during the last 50 hours are edged in black.

For comparison purposes, Fig. 3c shows the example of a much less structured FTLE field on 11 June 2016 (03:00) after persistently moderate winds from northerly directions. In this case sharp FTLE ridges are nearly absent. Overlaid to the FTLE field, Fig. 3c includes direct counterparts of the trajectories shown in Fig. 3b, released at exactly the same locations. Contrary to the situation in Fig. 3b, now all neighbouring trajectories are very much alike, mainly shifted in agreement with the slightly different release points. A similar behaviour occurs also at the time of Fig. 3b when particles are released away from the FTLE ridges (see Fig. S1 in the supplement).

3.3 Third example

29 February 2016 (Fig. 4a) provides another example of weak winds that follow more stormy conditions. At about 26 February, strong winds to the south of an atmospheric low make way for weaker winds under the influence of a high pressure system. Different from the previous example, however, the strong winds some days ago persistently blew from the west rather than from the east. Again a net of sharp FTLE ridges can be observed in Fig. 4a.

Figs. 4b and 4c analyse the situation in terms of statistical dispersion measures. Fig. 4b displays the spatial distribution of absolute dispersion. Each pixel in the plot represents the squared distance between the corresponding trajectory's release and end point. The plot reveals some sharp demarcations between zones with either broadly similar or at most smoothly changing drift velocities. A measure that directly concentrates on small scale changes in drift behaviour is two-particle relative dispersion (Fig. 4c). Its distribution closely resembles the FTLE field in Fig. 4a. Also the two maps of absolute and relative dispersion are in very good agreement, relative dispersion highlighting sharp transitions in the graph of absolute dispersion.

Fig. 4b also includes some example trajectories. Test trajectories near the horizontal divide south of MARNET station 4 illustrate a stepwise change of advection speed, giving rise to the enhanced level of absolute dispersion for the test station located more to the south (green). Note that a pure change of drift direction, maintaining advection speed, would have affected relative but not absolute dispersion. Three additional magenta trajectories, seeded at MARNET stations 1, 2 and 6, were included to just visualize spatial variability of transports.

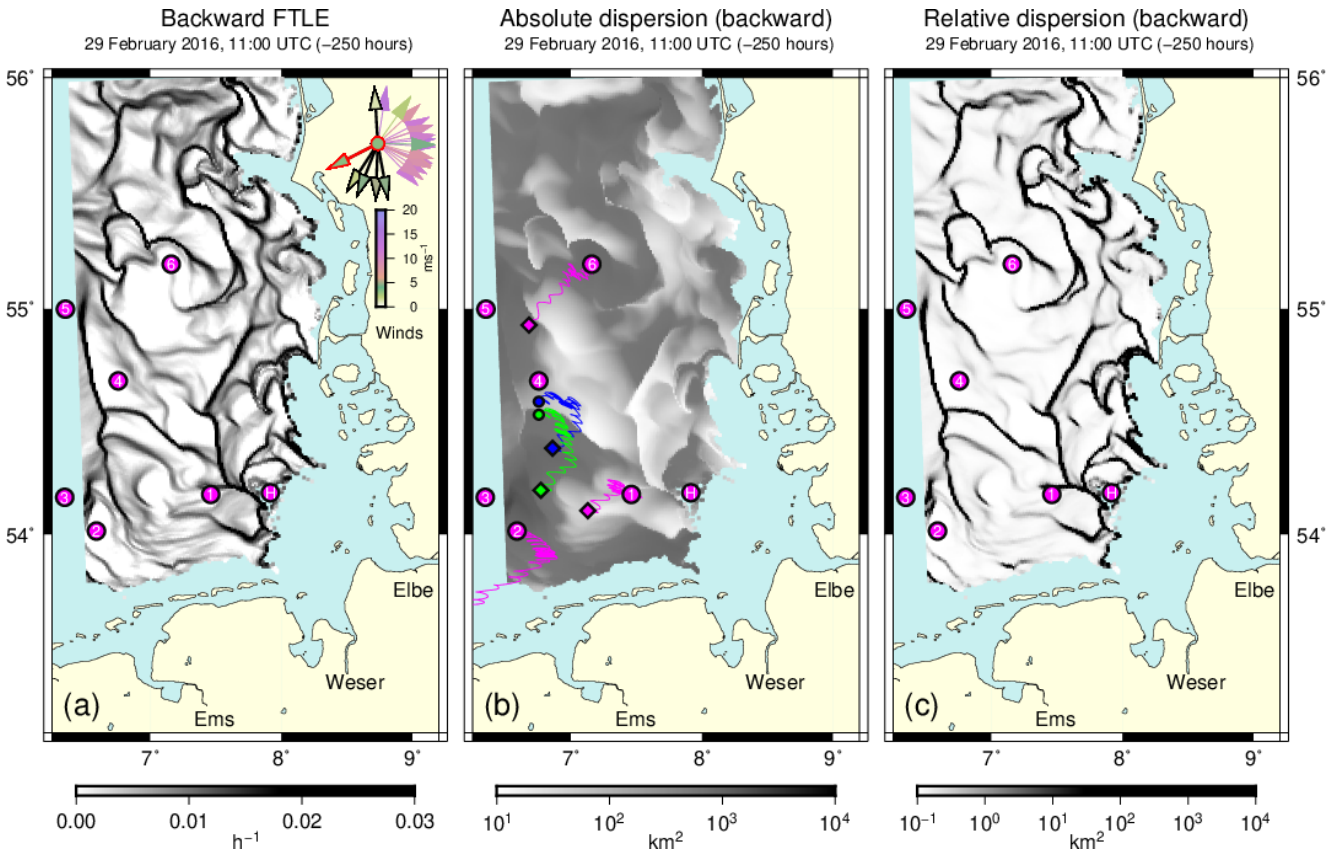

Figure 4. (a) Backward FTLE field (integration time 250 h) for 29 Feb 2016 (11:00). Magenta circles indicate locations of MARNET stations (1-6) and of the island of Helgoland (H). Vectors in the top right corner show past wind directions (modelled for the location of station 4) at ten hourly intervals. Different wind speeds are represented by a colour map. The wind vector at the time of the plot is edged in red, those during the last 50 hours are edged in black. **(b)** Absolute dispersion (backward squared particle displacements) for the same time. Example trajectories shown were initialized at MARNET monitoring stations 1, 2 and 6 (magenta) and at two locations (small circles in blue and green) neighbouring MARNET station 4 to its south. Small diamonds indicate each trajectory's final location. **(c)** Distribution of relative dispersion for the same time.

3.4 Fourth example

A video in the supplement, based on one FTLE field every 7 hours, shows the variability of FTLE ridges throughout 2016. The three panels of Fig. 5, extracted from this video, illustrate the development within the two week period 22 November to 6 December 2016.

Fig. 5a shows the situation after 10 days of mostly strong winds from between southeast and west. The FTLE field is much less compartmentalized than the fields in Figs. 3a and 4b, for instance. Instead it shows long FTLE ridges aligned in a meridional direction, resembling the situation in Fig. 2a. On 23 November, winds change from southern winds to winds from northern directions. This entails a reversal of the formerly pronounced cyclonic to an anticyclonic marine residual circulation[2]. The wind rose in Fig. 5b (27 November, 21:00) clearly clusters strong winds from the south underlying the period covered by FTLEs in Fig. 5a and winds from the north more recently. It can be seen how this transition of winds generates structures including also more east-west oriented ridges. After 3 December, a high pressure area with very low winds extends into the North Sea region. Under such calm conditions, the FTLE field in Fig. 5c suggests evolution towards a more cellular structure.

[2]see https://www.bsh.de/DE/DATEN/Stroemungen/Zirkulationskalender/zirkulationskalender_node.html

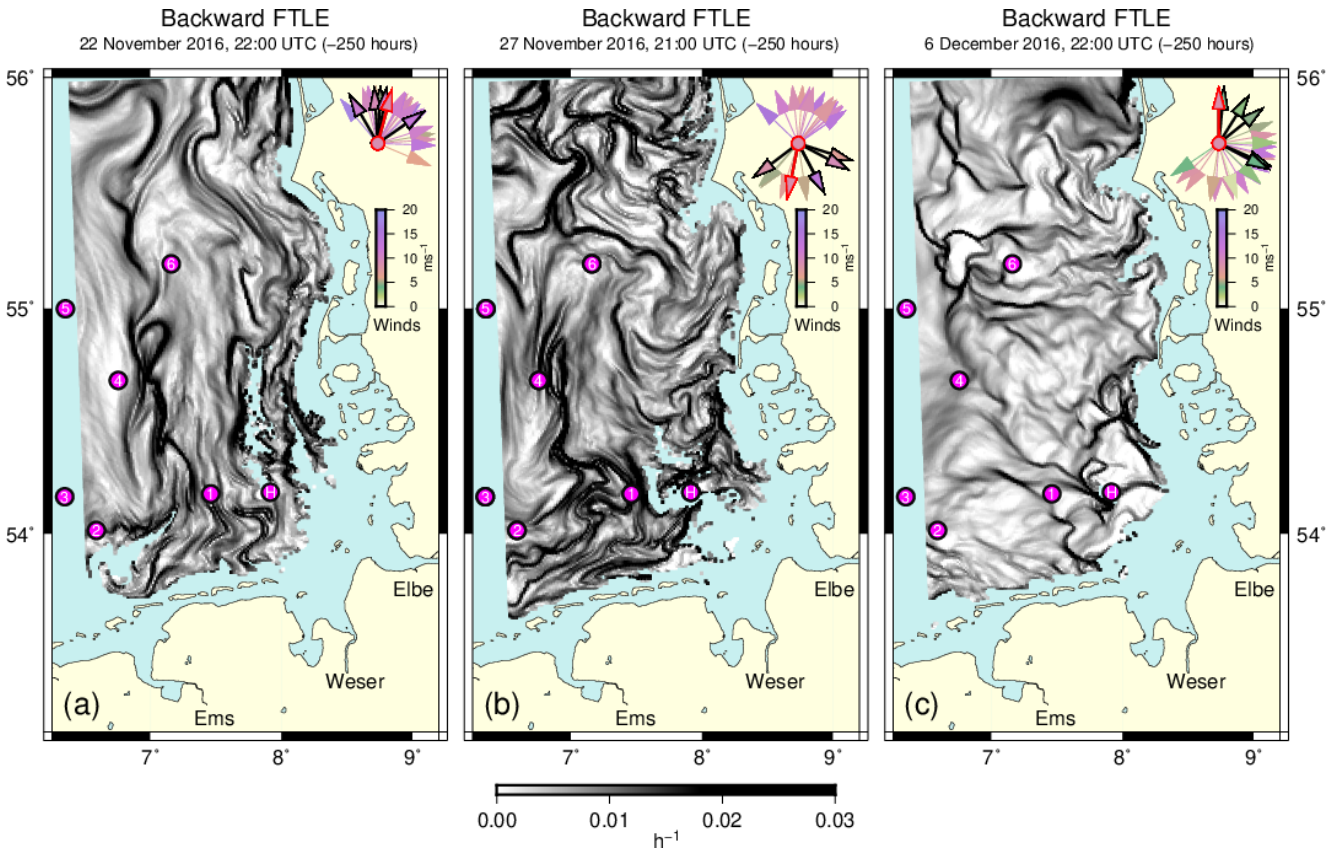

Figure 5. Three backward FTLE fields scheduled with approximately five and nine days in between, extracted from a video available in the supplement. Magenta circles indicate locations of MARNET stations (1-6) and of the island of Helgoland (H). Vectors in the top right corners show past wind directions (modelled for the location of station 4) at ten hourly intervals. Different wind speeds are represented by a colour map. Wind vectors at the respective times of the plots are edged in red, those during the last 50 hours are edged in black.

4 Discussion

Taking a monitoring perspective, this study focussed on the analysis of attracting LCSs, technically identified as repelling LCSs in backward simulations. Drift simulations based on BSHcmod surface layer currents revealed a pronounced time variability of LCSs, driven by the recent history of wind conditions. Some LCSs, identified as ridges in the FTLE field, were found to be surprisingly sharp (e.g. Figs. 3b or 4a), so that measurements at neighbouring locations might see water bodies with very different backgrounds. Similarly, at a given station, even a small wind-induced displacement of the FTLE field could substantially shift the origins of water bodies being probed. Being aware of such sensitivities can be relevant for a proper interpretation of observational data. Ridges in the simulated backward FTLE field convey the information in a clear and amenable way.

The general idea followed here differs from the objective of Ricker and Stanev (2020), for instance, who aimed at the identification of mean particle accumulation patterns (in forward mode) in the European northwest shelf on time scales of months or years. In the light of time-dependent, sometimes narrow FTLE ridges, the general characterization of monitoring stations in terms of their areas of influence seems difficult to achieve. Duran et al. (2018) derived climatological LCSs (cLCS) based on low-pass filtered velocity fields. These cLCSs could then successfully be applied for a description of quasi-steady transport patterns in the Gulf of Mexico. Marine currents in the German Bight area, however, are much more variable. Therefore, this study suggests the use of detailed numerical simulations to classify probed water bodies with regard to their presumable source regions. Similarly, detailed transport modelling could support the effective organization of field experiments. Not looking into the future, backward FTLE fields can be simulated already at the time when observations are actually taken. Such timely model based information on existing LCSs would allow for an adjustment of field campaigns to prevailing environmental conditions in the light of the data already gathered.

Examples shown suggest that in particular strong wind conditions trigger the occurrence of pronounced FTLE ridges, often being of considerable length or demarcating a net of closed subregions. These ridges continue to exist for some time also under subsequent calmer wind conditions (e.g. Figs. 3a and 3b). Throughout this study, all FTLE values were calculated based on trajectories integrated 250 hours back in time. This integration time is much longer than just few tidal cycles which, for instance, Orre et al. (2006) chose for analysing topographically constrained currents in a Norwegian fjord. Huhn et al. (2012) chose 24 hours for their study in the Ria de Vigo estuary, thereby preventing particles from reaching the boundaries. In the present study, all trajectories that met water depths below 5 m were discarded. The long integration time implied that even when being started under calm atmospheric conditions, trajectories experienced the storm event at the end of their backward integration. A very interesting observations is, however, that with integration time being reduced to just 50 or even 25 hours, the key FTLE ridges tended to become less sharp but did not disappear (see Fig. S2, demonstrating that for the example shown in Fig. 3b). This finding is consistent with the fact that example backward trajectories in Figs. 2a and 3b, for instance, show high drift velocities towards the end of the integration period but at the same time a clear separation of neighboured trajectories already right from the start. This proves a certain memory after the storm has ceased.

In this study, FTLE fields were analysed on a 1 km grid, nearly matching resolution of the marine current fields. Computationally more demanding FTLE analyses on a finer grid would have enabled identification of structures even smaller than resolution of the Eulerian hydrodynamic model arising, however, from tracer simulations over longer distances (Huhn et al., 2012). This shows that a classification of kinematic LCSs in terms of mesoscale or submesoscale features and processes may be difficult. Longer integration periods underlying the LCS analysis may filter more short-term features (Serra and Haller, 2016).

In their study of Lagrangian transports in the Gulf of Mexico, Duran et al. (2018) found patterns shaping two-dimensional transports to arise from merely confluence, i.e. normal attraction and tangential stretching without convergence. Similarly, Lehahn et al. (2007) found satellite observations of chlorophyll filaments in the northeast Atlantic to well agree with simulated geostrophic transports, contracting at and stretching along material lines. Referring to Lapeyre and Klein (2006), they argue that an ageostrophic secondary circulation injecting nutrients from deeper layers may trigger further chlorophyll production. Similarly, Olascoaga et al. (2013, their Fig. 1) provide an example of how a chlorophyll a plume in the Gulf of Mexico coincides with a divergence-free attracting LCS. At the smaller submesoscale, however, Hernández-Carrasco et al. (2018) found negative extremes of Lagrangian divergence to coincide with attracting LCSs identified as ridges in the field of backward Finite-Size Lyapunov Exponents (FSLE) analysed from HF radar data. Also in the present study, fields of path-averaged finite-domain Lagrangian divergence FDLD suggested the role of backward FTLE ridges as lines of convergence in coastal waters. This was explicitly shown for the example in Fig. 2 but pertains also to all the other examples.

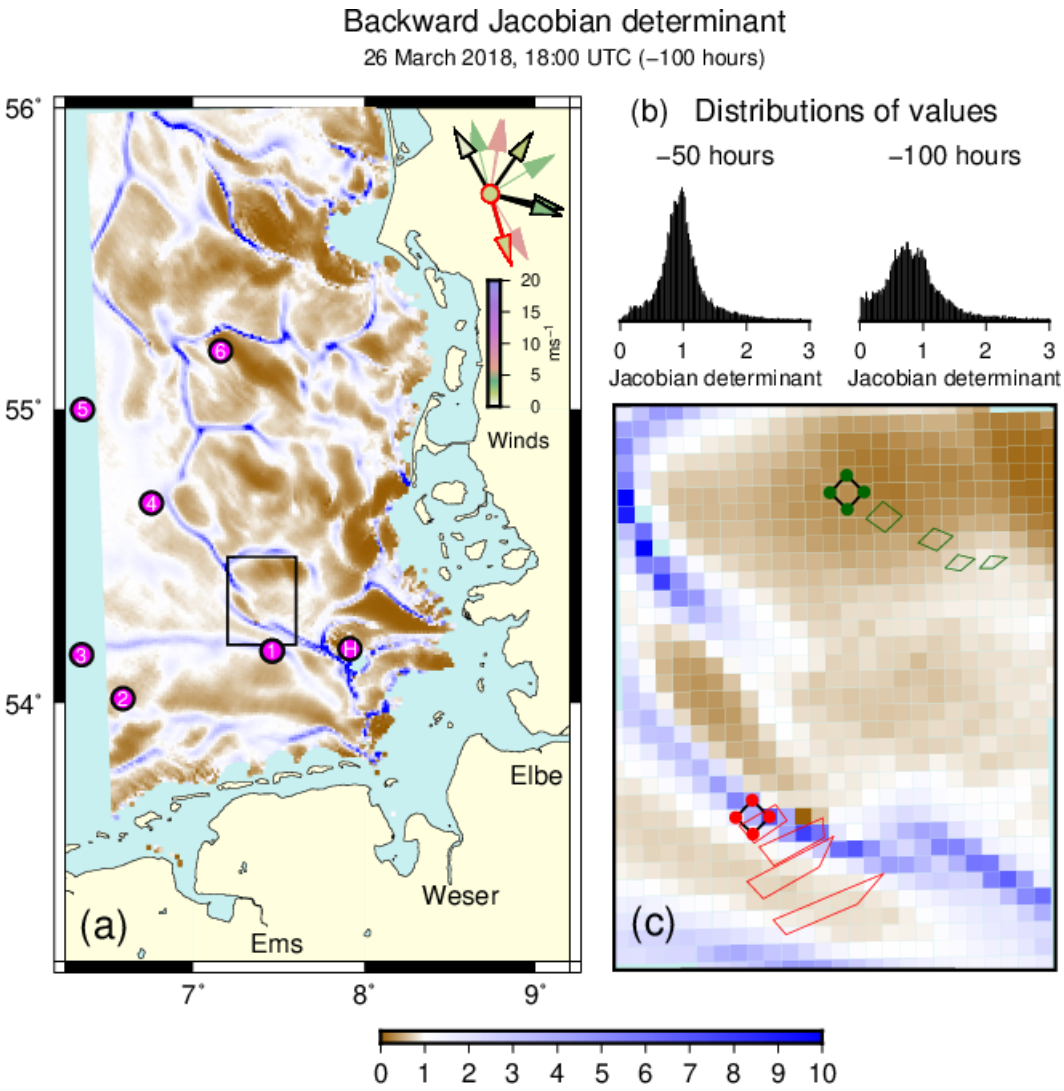

Figure 6. (a) Values of the Jacobian determinant (Eq. (4)) for 100 h backward simulations, initialized on 26 March 2018 (as in Fig. 3b). Few outliers exceeding the maximum value of the colour map were not specifically marked. Any negative values, possible due to finite initial distances, were omitted in the plot. Wind directions during integration time are shown at ten hourly intervals in the top right corner of the panel. The actual wind vector is edged in red, those during the last 50 hours are edged in black. **(b)** Histograms of Jacobian determinant values for integration times -50 h (left) and -100 h (right), respectively. Note that the distributions' flat tales extend beyond the ranges of values being shown. **(c)** Zooming in on the subregion indicated by the black frame in panel (a), the panel shows the time evolution of two square patches, corners of which are made up by the initial locations (red and green dots) of the four trajectories needed to calculate the discretized deformation gradient (Eq. (2)) at the respective square's center. Deformed quadrangles emerging during the -100 h integration period are shown at 25 hourly intervals. Factors of area in- or decreases $\mu_1\mu_2$ (Eq. (3)) are 1.56, 2.50, 3.40, 3.73 (red) and 0.96, 0.70, 0.42, 0.31 (green), where the last values equal the values for -100 h shown in the map. Corresponding stretches μ_1/μ_2 (see Eq. (6)) are 1.88, 3.01, 3.78, 5.52 (red) and 1.17, 1.52, 1.98, 2.36. (green).

Referring to the example addressed in Fig. 3b, Fig. 6a shows the corresponding field of the Jacobian determinant. A shorter integration period of only -100 h (rather than -250 h) was chosen to exclude the period of strong easterly winds that occurred about 8 days before the date of the analysis (compare the wind roses in Fig. 3b and Fig. 6a, respectively). Despite the shortened integration time, ridges in the backward Jacobian determinant field well coincide with FTLE ridges in Fig. 3b. Values of the Jacobian determinant are substantially spread around the neutral value of one that corresponds with zero divergence (Fig. 6b). Values further spread with increasing integration time. To exemplify patterns of transport, Fig. 6c shows the development of two patches with either increasing or decreasing area. At each time level, the quadrangles are defined by the positions of the four trajectories that emerge from the locations used to calculate the discretized deformation radius (Eq. (2)) in their centre. The more southern example emerges from a location on a ridge in the Jacobian determinant field. After 100 hours back in time, the initial area has grown by a factor of 3.73, which equals the values of the determinant shown in the map. By contrast, starting from the more northern example location, the area decreases by a factor of 0.31. In both example cases the drift behaviour is far from being non-divergent.

In both cases, however, also substantial stretching occurs. Final stretches μ_1/μ_2 of the example squares in Fig. 6c amount to 5.52 (red) and 2.36 (green). To differentiate the effects of divergent flows from divergence-free repulsion, Huntley et al. (2015) introduced the decomposition of the FTLE measure into dilation rate Δ and stretch rate Σ (see Section 2.5). For the three examples presented in Fig. 2, Fig. 3b and Fig. 4, respectively, Table 1 provides the correlations between FTLE and either dilation Δ or stretch rate Σ. In each case, correlations are given for the three different integration times of -50 h, -100 h and -250 h, respectively. Both correlations between FTLE and Δ or Σ are generally positive and of similar size, indicating that repulsion in the vicinity of backward FTLE ridges indeed occurs as a combination of divergence and stretching. In all three examples, an interesting observation is that the correlations between FTLE and dilation rate Δ increase with integration time, while correlations with stretch rate Σ decrease. As a result, correlation of FTLE values with dilation rate Δ is dominant for the -250 h integration time chosen in this study.

The temperature field in Fig. 2c provided an indication of confluent and possibly also convergent currents. Surface temperature observations by remote sensing might possibly provide a means to confirm simulated FDLD fields. Schrum (1997) showed how the spatial extent of thermohaline stratified areas, a precondition for the occurrence of tidal mixing fronts, depends on wind forcing that possibly induces differential advection. In a recent paper, Chegini et al. (2020) provided a more detailed analysis of different processes that affect stratification and destratification in the German Bight area, including freshwater buoyancy input. Location of the Elbe River plume again depends on the wind driven residual circulation, which further substantiates the assumption of atmospheric forcing being a key driver for the generation, movement and extinction of German Bight LCSs.

Relatively persistent FTLE ridges related to the island of Helgoland, for instance, could possibly be relevant for sedimentation processes. However, movements of inertial tracers can substantially differ from those of fluid parcels, so that an analysis of ideal passive tracer trajectories is likely to be too simplistic in that context. The idea of LCSs has been generalized, however, to explicitly include the dynamics of inertial particles (Sapsis and Haller, 2009; Sudharsan et al., 2016; Günther and Theisel, 2017). This theoretical concept has successfully been applied on the scale of ocean eddies (Beron-Vera et al., 2015) but also on the very small scale of jellyfish feeding (Peng and Dabiri, 2009; Sapsis et al., 2011).

Table 1. Correlations between FTLE and its additive components Δ and Σ (see Eq.8).

	τ	12 Jun 2015 (Fig. 2)	26 Mar 2018 (Fig.3b)	29 Feb 2016 (Fig. 4)
corr (FTLE, Δ)	-50 h	0.41	0.59	0.68
	-100 h	0.51	0.66	0.73
	-250 h	0.65	0.72	0.77
corr (FTLE, Σ)	-50 h	0.69	0.63	0.57
	-100 h	0.65	0.57	0.47
	-250 h	0.52	0.50	0.37

For three examples presented in this paper, the table shows correlations obtained for backward integration times τ=-50 h, -100 h and -250 h, respectively.

Although numerical models can make observers aware of FTLE barries that move, disappear or newly arise under changing environmental conditions, they can never provide a perfect surrogate nature. Guo et al. (2016) propose concepts to extend the conventional analysis of deterministic FTLE fields and ridges to uncertain flow conditions. In a comparative study, Hufnagl et al. (2017) found considerable discrepancies between the results from a large number of different North Sea tracer simulations essentially based on vertical mean currents. Wiggins (2005) makes reservations that, as contrasted with many engineering applications, the presence and interaction of very different scales in geophysical flows can restrict the possibility of simulating detailed particle drift paths. Altogether, simulated FTLE field will always be imperfect. However, even in case of inaccurate simulations, simulated FTLE fields will warn users about key sensitivities of specific model output. If an observation is taken close to a simulated FTLE ridge, a simulated backward trajectory for this location must be used with due care.

This study did not address repelling LCSs in prediction (forward) mode. Drift simulations are important tools employed for search and rescue (SAR), for instance (Breivik et al., 2013). Serra et al. (2020) proposed the use of objective Eulerian coherent structures (OECS) in this context, a concept developed by Serra and Haller (2016) for being used when quick operational decisions are to be made. According to Serra and Haller (2016), OECSs can be understood as short-time limits of LCSs, applicable for a time horizon of very few hours. More long-term forward simulations are feasible and can be afforded in the context of ecosystem hindcasts, analysing larval transport and dispersal, for instance.

For surface drift simulations, additional uncertainties may arise from the necessity to specify the extent to which near surface currents are exposed to a direct wind drag. Callies et al. (2017b, 2019) found that a successful simulation of observed drifter trajectories needed BSHcmod surface currents to be augmented by a leeway of 0.6 % of 10 m winds. Besides a small direct wind drag exerted on the drifters themselves, this leeway compensates for insufficient vertical resolution in the archived surface current fields (representing a layer of 5 m depth). In addition, the leeway may also parameterize wave related Stokes drift not being considered explicitly (Callies et al., 2017b; Sutherland et al., 2020). Example forward FTLE fields including a 6 %

leeway are shown in Fig. S3. The example shows that FTLE ridges are modified but do not disappear when the smooth fields of a wind induced leeway are superimposed to marine currents. This conclusion directly translates to all the backward FTLE fields analysed in this paper.

5 Conclusions

The analysis of backward surface tracer simulations in the German Bight region revealed the intermittent presence of linear structures (LCSs) across which the past history of water bodies substantially changes. Such sensitive dependences of backward trajectories on tracer seeding positions, represented by narrow ridges in the FTLE field, could entail differences between in situ observations even at neighbouring locations. Therefore, an evaluation of spatially distributed in situ observations could benefit from the awareness of changing FTLE fields, analysed based on either numerical simulations or possibly high frequency (HF) radar observational data.

In the presence of narrow FTLE ridges, marked differences between observed and simulated tracer trajectories do not necessarily reflect poor model performance. If the location of a simulated LCS does not fully agree with reality, a tracer release point may come to lie on different sides of the separatrices in the model and in nature, respectively. In this case, a naive comparison of trajectories could much exaggerate inconsistencies. The same arguments pertain to a comparison of different drift models. Therefore, conventional model evaluations based on individual drift paths might be complemented with a comparison of simulated FTLE fields.

Examples illustrated the variability of German Bight surface layer LCSs under changing wind conditions. For a more comprehensive picture it could be useful to establish a formal model that estimates the basic characteristics of backward FTLE fields, given a recent history of atmospheric forcing. The examples studied suggest that model uncertainties occur particularly in the aftermath of storm conditions. Due to the presence of sometimes complex filamentary structures, a decomposition of FTLE fields in terms of a mean plus a number of weighted anomaly fields seems not very promising. Classification of FTLE fields into a limited number of categories could be useful. This problem is left to future research.

Code and data availability. The hydrodynamic data analysed in this paper were obtained from the repository of the Federal Maritime and Hydrographic Agency (BSH). For access to the archived results of the operational hydrodynamical model BSHcmod, please contact BSH (www.bsh.de). The Lagrangian drift code PELETS is available on request from the author.

Video supplement. A video is provided (FTLE_2016.avi) that demonstrates the temporal development of FTLE fields in the course of the year 2016, based on FTLE fields calculated every 7 hours.

Author contributions. The author performed all analyses and prepared the manuscript.

Competing interests. The author declares that he has no conflict of interest.

Acknowledgements. Drift simulations were based on BSHcmod currents provided by the Federal Maritime and Hydrographic Agency (BSH). Graphs were produced using the Generic Mapping Tools software (GMT) available from www.soest.hawaii.edu/gmt/. I would like to thank Rodrigo Duran for some helpful suggestions. I furthermore appreciate comments by Jens Meyerjürgens and two anonymous referees.

References

Aurell, E., Boffetta, G., Crisanti, A., Palatin, G., and Vulpiani, A.: Growth of noninfinitesimal perturbations in turbulence, Phys. Rev. Lett., 77, 1262–1265, https://doi.org/10.1103/PhysRevLett.77.1262, 1996.

Aurell, E., Boffetta, G., Crisanti, A., Palatin, G., and Vulpiani, A.: Predictability in the large: an extension of the concept of Lyapunov exponent, J. Phys. A, 30, 1–26, https://doi.org/10.1088/0305-4470/30/1/003, 1997.

Baschek, B., Schroeder, F., Brix, H., Riethmüller, R., Badewien, T. H., Breitbach, G., Brügge, B., Colijn, F., Doerffer, R., Eschenbach, C., Friedrich, J., Fischer, P., Garthe, S., Horstmann, J., Krasemann, H., Metfies, K., Merckelbach, L., Ohle, N., Petersen, W., Pröfrock, D., Röttgers, R., Schlüter, M., Schulz, J., Schulz-Stellenfleth, J., Stanev, E., Staneva, J., Winter, C., Wirtz, K., Wollschläger, J., Zielinski, O., and Ziemer, F.: The Coastal Observing System for Northern and Arctic Seas (COSYNA), Ocean Sci., 13, 379–410, https://doi.org/10.5194/os-13-379-2017, https://www.ocean-sci.net/13/379/2017/, 2017.

Becker, G. A., Dick, S., and Dippner, J. W.: Hydrography of the German Bight, Mar. Ecol. Prog. Ser., 91, 9–18, 1992.

Beron-Vera, F. J., Olascoaga, M. J., Haller, G., Farazmand, M., Triñanes, J., and Wang, Y.: Dissipative inertial transport patterns near coherent Lagrangian eddies in the ocean, Chaos, 25, 087 412, https://doi.org/10.1063/1.4928693, 2015.

Breivik, Ø., Allen, A. A., Maisondieu, C., and Olagon, M.: Advances in search and rescue at sea, Ocean Dyn., 63, 83–88, https://doi.org/10.1007/s10236-012-0581-1, 2013.

Budéus, G.: Frontal variability in the German Bight, Sci. Mar., 53, 175–185, 1989.

Callies, U., Plüß, A., Kappenberg, J., and Kapitza, H.: Particle tracking in the Vicinity of Helgoland, North Sea: A Model Comparison, Ocean Dyn., 61, 2121–2139, https://doi.org/10.1007/s10236-011-0474-8, 2011.

Callies, U., Gaslikova, L., Kapitza, H., and Scharfe, M.: German Bight residual current variability on a daily basis: principal components of multi-decadal barotropic simulations, Geo-Mar. Lett., 37, 151–162, https://doi.org/10.1007/s00367-016-0466-2, 2017a.

Callies, U., Groll, N., Horstmann, J., Kapitza, H., Klein, H., Maßmann, S., and Schwichtenberg, F.: Surface drifters in the German Bight: model validation considering windage and Stokes drift, Ocean Sci., 13, 799–827, https://doi.org/10.5194/os-13-799-2017, 2017b.

Callies, U., Carrasco, R., Floeter, J., Horstmann, J., and Quante, M.: Submesoscale dispersion of surface drifters in a coastal sea near offshore wind farms, Ocean Sci., 15, 865–889, https://doi.org/10.5194/os-15-865-2019, 2019.

Chegini, F., Holtermann, P., Kerimoglu, O., Becker, M., Kreus, M., Klingbeil, K., Gräwe, U., Winter, C., and Burchard, H.: Processes of stratification and destratification during an extreme river discharge event in the German Bight ROFI, J. Geophys. Res.: Oceans, 125, e2019JC015 987, https://doi.org/10.1029/2019JC015987, 2020.

Chen, K., Ni, M., Cai, M., Huang, J. W. D., Chen, H., Wang, X., and Liu, M.: Optimization of a coastal environmental monitoring network based on the Kriging method: A case study of Quanzhou Bay, China, Biomed. Res. Int., 2016, Article ID 7137 310, https://doi.org/10.1155/2016/7137310, 2016.

Dick, S., Kleine, E., Müller-Navarra, S., Klein, H., and Komo, H.: The operational circulation model of BSH (BSHcmod). Model description and validation, Tech. Rep. 29/2001, BSH, 2001.

Dick, S., Kleine, E., and Janssen, F.: A new operational circulation model for the North Sea and Baltic Sea using a novel vertical coordinate setup and first results, in: Coastal to Global Operational Oceanography: Achievements and Challenges. Proceedings of the Fifth International Conference on EuroGOOS, 20-22 May 2008, Exeter, UK, edited by Dalhin, H., Bell, M. J., Flemming, N. C., and Petersen, S. E., 2008.

d'Ovidio, F., De Monte, S., Alvain, S., Dandonneau, Y., and Lévy, M.: Fluid dynamical niches of phytoplankton types, PNAS, 107, 18 366–18 370, https://doi.org/10.1073/pnas.1004620107, 2010.

d'Ovidio, F., Penna, A. D., Trull, T. W., Nencioli, F., Pujol, M.-I., Rio, M.-H., Park, Y.-H., Cotté, C., Zhou, M., and Blain, S.: The biogeochemical structuring role of horizontal stirring: Lagrangian perspectives on iron delivery downstream of the Kerguelen Plateau, Biogeosciences, 12, 5567–5581, https://doi.org/10.5194/bg-12-5567-2015, 2015.

Duran, R., Beron-Vera, F. J., and Olascoaga, M. J.: Extracting quasi-steady Lagrangian transport patterns from the ocean circulation: An application to the Gulf of Mexico, Scientific Reports, 8:5218, 9, https://doi.org/10.1038/s41598-018-23121-y, 2018.

Farazmand, M. and Haller, G.: Comuputing Lagrangian coherent structures from their variational theory, Chaos, 22, 013 128, https://doi.org/10.1063/1.3690153, 2012.

Günther, T. and Theisel, H.: Backward finite-time Lyapunov exponents in inertial flows, IEEE Trans. Vis. Comput. Graph., 23, 970–979, https://doi.org/10.1109/TVCG.2016.2599016, 2017.

Guo, H., He, W., Peterka, T., Shen, H.-W., Collis, S. M., and Helmus, J. J.: Finite-time Lyapunov exponents and Lagrangian coherent structures in uncertain unsteady flows, IEEE Trans. Vis. Comput. Graph., 22, 1672–1682, https://doi.org/10.1109/TVCG.2016.2534560, 2016.

Hadjighasem, A., Farazmand, M., Blazevski, D., Froyland, G., and Haller, G.: A critical coparison of Lagrangian methods for coherent structure detection, Chaos, 27, 053 104, https://doi.org/10.1063/1.4982720, 2017.

Haller, G.: Distinguished material surfaces and coherent structures in three-dimensional fluid flows, Physica D, 149, 248–277, https://doi.org/10.1016/S0167-2789(00)00199-8, 2001.

Haller, G.: A variational theory of hyperbolic Lagrangian coherent structures, Physica D, 240, 574–598, https://doi.org/10.1016/j.physd.2010.11.010, 2011.

Haller, G.: Lagrangian coherent structures, Annu. Rev. Fluid Mech., 47, 137–162, https://doi.org/10.1146/annurev-fluid-010313-141322, 2015.

Haller, G. and Yuan, G.: Lagrangian coherent structures and mixing in two-dimensional turbulence, Physica D, 147, 352–370, https://doi.org/10.1016/S0167-2789(00)00142-1, 2000.

Harrison, C. S. and Glatzmaier, G. A.: Lagrangian coherent structures in the California Current System - sensitities and limitations, Geophys. Astro. Fluid Dyn., 106, 22–44, https://doi.org/10.1080/03091929.2010.532793, 2010.

Hernández-Carrasco, I., Orfila, A., Rossi, V., and Garçon, V.: Effect of small scale transport processes on phytoplankton distribution in coastal seas, Scientific Reports, 8, 8613, https://doi.org/10.1038/s41598-018-26857-9, 2018.

Holt, J. and Umlauf, L.: Modelling the tidal mixing fronts and seasonal stratification of the Northwest European Continental shelf, Cont. Shelf Res., 28, 887–903, https://doi.org/10.1016/j.csr.2008.01.012, 2008.

Hufnagl, M., Payne, M., Lacroix, G., Bolle, L. J., Daewel, U., Dickey-Collas, M., Gerkema, T., Huret, M., Janssen, F., Kreus, M., Pätsch, J., Pohlmann, T., Ruardij, P., Schrum, C., Skogen, M. D., Tiessen, M. C., Petitgas, P., van Beek, J. K., van der Veer, H. W., and Callies, U.: Variation that can be expected when using particle tracking models in connectivity studies, J. Sea Res., 127, 133–149, https://doi.org/10.1016/j.seares.2017.04.009, 2017.

Huhn, F., von Kameke, A., Allen-Perkins, S., Montero, P., Venancio, A., and Pérez-Muñuzuri, V.: Horizontal Lagrangian transport in a tidal-driven estuary - Transport barriers attached to prominent coastal boundaries, Cont. Shelf Res., 39-40, 1–13, https://doi.org/10.1016/j.csr.2012.03.005, 2012.

Huntley, H. S., Lipphardt, B. L., Jacobs, G., and Kirwan Jr., A. D.: Clusters, deformation, and dilation: Diagnostics for material accumulation regions, J. Geophys. Res., 120, 6622–6636, https://doi.org/10.1002/2015JC011036, 2015.

James, I. D.: A three-dimensional numerical shelf-sea front model with variable eddy viscosity and diffusivity, Cont. Shelf Res., 3, 69–98, 1984.

Karrasch, D. and Haller, G.: Do finite-size Lyapunov exponents detect coherent structures?, Chaos, 23, 043 126, https://doi.org/10.1063/1.4837075, 2013.

Kim, N.-H. and Hwang, J. H.: Optimal design of water quality monitoring networks in semi-enclosed estuaries, Sensors, 20, 1498, https://doi.org/10.3390/s20051498, 2020.

Krause, G., Budeus, G., Gerdes, D., Schaumann, K., and Hesse, K.: Frontal systems in the German Bight and their physical and biological effects, in: Marine Interfaces Ecohydrodynamics, edited by Nihoul, J. C. J., pp. 119–140, Elsevier, Amsterdam, 1986.

LaCasce, J. H.: Statistics from Lagrangian observations, Prog. Oceanogr., 77, 1–29, https://doi.org/10.1016/j.pocean.2008.02.002, 2008.

LaCasce, J. H. and Ohlmann, C.: Relative dispersion at the surface of the Gulf of Mexico, J. Mar. Res., 61, 285–312, https://doi.org/10.1357/002224003322201205, 2003.

Lapeyre, G. and Klein, P.: Impact of the small-scale elongated filaments on the oceanic vertical pump, J. Mar. Res., 64, 835–851, https://doi.org/10.1357/002224006779698369, 2006.

Lehahn, Y., d'Ovidio, F., Lévy, M., and Heifetz, E.: Stirring of the northeast Atlantic spring bloom: A Lagrangian analysis based on multi-satellite data, J. Geophys. Res., 112, C08 005, https://doi.org/10.1029/2006JC003927, 2007.

Lucas, J., Koester, I., Wichels, A., Niggemann, J., Dittmar, T., Callies, U., Wiltshire, K. H., and Gerdts, G.: Short-term dynamics of North Sea bacterioplankton-dissolved organic matter coherence on molecular level, Front. Microbiol., 7:321, https://doi.org/10.3389/fmicb.2016.00321, 2016.

Meyerjürgens, J., Ricker, M., Schakau, V., Badewien, T. H., and Stanev, E. V.: Relative dispersion of surface drifters in the North Sea: The effect of tides on mesoscale diffusivity, JGR Oceans, 124, e2019JC015925, https://doi.org/10.1029/2019JC015925, 2020.

Molcard, A., Andrew C, P., and Özgökmen, T. M.: Directed drifter launch strategies for Lagrangian data assimilation using hyperbolic trajectories, Ocean Model., 12, 268–289, https://doi.org/10.1016/j.ocemod.2005.06.004, 2006.

Olascoaga, M. J., Beron-Vera, F. J., Haller, G., Triñanes, J., Iskandarani, M., Coelho, E. F., Haus, B. K., Huntley, H. S., Jacobs, G., Kirwan Jr., A. D., Lipphardt Jr., B. L., Özgökmen, T. M., Reniers, A. J. H., and Valle-Levinson, A.: Drifter motion in the Gulf of Mexico constrained by altimetric Lagrangian coherent structures, Geophys. Res. Lett., 40, 6171–6175, https://doi.org/10.1002/2013GL058624, 2013.

Orre, S., Gjevik, B., and LaCasce, J. H.: Characterizing chaotic dispersion in a coastal tidal model, Cont. Shelf Res., 26, 1360–1374, https://doi.org/10.1016/j.csr.2005.11.015, 2006.

Peacock, T. and Haller, G.: Lagrangian coherent structures: the hidden skeleton of fluid flows, Phys. Today, 66, 41–47, https://doi.org/10.1063/PT.3.1886, 2013.

Peng, J. and Dabiri, J. O.: Transport of inertial particles by Lagrangian coherent structures: application to predator-prey interaction in jellyfish feeding, J. Fluid Mech., 623, 75–84, https://doi.org/10.1017/S0022112008005089, 2009.

Pierrehumbert, R. T. and Yang, H.: Global chaotic mixing on isentropic surfaces, J. Atmos. Sci., 50, 2462–2480, https://doi.org/10.1175/1520-0469(1993)050<2462:GCMOIS>2.0.CO;2, 1993.

Poje, A. C., Toner, M., Kirwan Jr., A. D., and Jones, C. K. R. T.: Drifter launch strategies based on Lagrangian templates, J. Phys. Oceanogr., 32, 1855–1869, https://doi.org/10.1175/1520-0485(2002)032<1855:DLSBOL>2.0.CO;2, 2002.

Press, W. H., Teukolsky, S. A., Vetterling, W. T., and Flannery, B. P.: Numerical Recipies in FORTRAN - The Art of Scientific Computing, Cambridge University Press, Cambridge, UK, 2 edn., 1992.

Ricker, M. and Stanev, E. V.: Circulation of the European northwest shelf: a Lagrangian perspective, Ocean Sci., 16, 637–655, https://doi.org/10.5194/os-16-637-2020, 2020.

Sansón, L. Z., Pérez-Brunius, P., and Sheinbaum, J.: Surface relative dispersion in the southwestern Gulf of Mexico, J. Phys. Oceanogr., 47, 387–403, https://doi.org/10.1175/JPO-D-16-0105.1, 2017.

Sapsis, T. and Haller, G.: Inertial particle dynamics in a hurricane, J. Atmos. Sci., 66, 2481–2492, https://doi.org/10.1175/2009JAS2865.1, 2009.

Sapsis, T., Peng, J., and Haller, G.: Instabilities on prey dynamics in jellyfish feeding, Bull. Math. Biol., 73, 1841–1856, https://doi.org/10.1007/s11538-010-9594-4, 2011.

Scales, K. L., Hazen, E. L., Jacox, M. G., Castruccio, F., Maxwell, S. M., Lewison, R. L., and Bograd, S. J.: Fisheries bycatch risk to marine megafauna is intensified in Lagrangian coherent structures, PNAS, 115, 7362–7367, https://doi.org/10.1073/pnas.1801270115, 2018.

Schrum, C.: Thermohaline stratification and instabilities at tidal mixing fronts: results of an eddy resolving model for the German Bight, Cont. Shelf Res., 17, 689–716, https://doi.org/10.1016/S0278-4343(96)00051-9, 1997.

Schulz, J.-P. and Schättler, U.: Kurze Beschreibung des Lokal-Modells Europa COSMO-EU (LME) und seiner Datenbanken auf dem Datenserver des DWD, https://www.dwd.de/SharedDocs/downloads/DE/modelldokumentationen/nwv/cosmo_eu/cosmo_eu_dbbeschr_201406.pdf?__blob=publicationFile&v=3, 2014.

Serra, M. and Haller, G.: Objective Eulerian coherent structures, Chaos, 26, 053 110, https://doi.org/10.1063/1.4951720, 2016.

Serra, M., Sathe, P., Rypina, I., Kirincich, A., Ross, S. D., Lermusiaux, P., Allen, A., Peacock, T., and Haller, G.: Search and rescue at sea aided by hidden flow structures, Nat Commun, 11, 2525, https://doi.org/10.1038/s41467-020-16281-x, 2020.

Shadden, S. C., Lekien, F., and Marsden, J. E.: Definition and properties of Lagrangian coherent structures from finite-time Lyapunov exponents in two-dimensional aperiodic flows, Physica D, 212, 271–304, https://doi.org/10.1016/j.physd.2005.10.007, 2005.

Shadden, S. C., Lekien, F., Paduan, J. D., Chavez, F. P., and Marsden, J. E.: The correlation between surface drifters and coherent structures based on high-frequency radar data in Monterey Bay, Deep-Sea Res. II, 56, 161–172, https://doi.org/10.1016/j.dsr2.2008.08.008, 2009.

Smagorinsky, J.: General circulation experiments with the primitive equations, I. the basic experiment, Mon. Weather Rev., 91, 99–164, https://doi.org/http://dx.doi.org/10.1175/1520-0493(1963)091<0099:GCEWTP>2.3.CO;2, 1963.

Smith, S. and Banke, E.: Variation of the sea surface drag coefficient with wind speed, Q. J. Roy. Meteor. Soc., 101, 665–673, https://doi.org/10.1002/qj.49710142920, 1975.

Stanev, E. V., Schulz-Stellenfleth, J., Staneva, J., Grayek, S., Grashorn, S., Behrens, A., Koch, W., and Pein, J.: Ocean forecasting for the German Bight: from regionalto coastal scales, Ocean Sci., 12, 1105–1136, https://doi.org/10.5194/os-12-1105-2016, 2016.

Stanev, E. V., Badewien, T. H., Freund, H., Grayek, S., Hahner, F., Meyerjürgens, J., Ricker, M., Schöneich-Argent, R. I., Wolff, J.-O., and Zielinski, O.: Extreme westward surface drift in the North Sea: Public reports of stranded drifters and Lagrangian tracking, Cont. Shelf Res., 177, 24–32, https://doi.org/10.1016/j.csr.2019.03.003, 2019.

Sudharsan, M., Brunton, S. L., and Riley, J. J.: Lagrangian coherent structures and inertial particle dynamics, Phys. Rev. E, 93, 033 108, https://doi.org/10.1103/PhysRevE.93.033108, 2016.

Sündermann, J. and Pohlmann, T.: A brief analysis of the North Sea physics, Oceanologia, 53, 663–689, https://doi.org/10.5697/oc.53-3.663, 2011.

Sutherland, G., Soontiens, N., Davidson, F., Smith, G. C., Bernier, N., Blanken, H., Schillinger, D., Marcotte, G., Röhrs, J., Dagestad, K.-F., Christensen, K. H., and Breivik, Ø.: Evaluating the leeway coefficient for different ocean drifters using operational models, arXiv:2005.09527 [physics.ao-ph], 2020.

Teeling, H., Fuchs, B. M., Becher, D., Klockow, C., Gardebrecht, A., Bennke, C. M., Kassabgy, M., Huang, S., Mann, A. J., Waldmann, J., Weber, M., Klindworth, A., Otto, A., Lange, J., Bernhardt, J., Reinsch, C., Hecker, M., Peplies, J., Bockelmann, F. D., Callies, U., Gerdts, G., Wichels, A., Wiltshire, K. H., Glöckner, F. O., Schweder, T., and Amann, R.: Substrate-controlled succession of marine bacterioplankton populations induced by a phytoplankton bloom, Science, 336(6081), 608–611, https://doi.org/10.1126/science.1218344, 2012.

Tian, F., He, Q., Liu, Z., and Chen, G.: Extracting Lagrangian coherent structures in the Kuroshio current system, Ocean Dyn., 69, 641–656, https://doi.org/10.1007/s10236-019-01262-6, 2019.

van Sebille, E., Griffies, S. M., Abernathey, R., Adams, T. P., Berloff, P., Biastoch, A., Blanke, B., Chassignet, E. P., Cheng, Y., Cotter, C. J., Deleersnijder, E., Döös, K., Drake, H. F., Drijfhout, S., Gary, S. F., Heemink, A. W., Kjellsson, J., Koszalka, I. M., Lange, M., Lique, C., MacGilchrist, G. A., Marsh, R., Mayorga Adame, C. G., McAdam, R., Nencioli, F., Paris, C. B., Piggott, M. D., Polton, J. A., Rühs, S., Shah, S. H., Thomas, M. D., Wang, J., Wolfram, P. J., Zanna, L., and Zika, J. D.: Lagrangian ocean analysis: Fundamentals and practices, Ocean Modelling, 121, 49 – 75, https://doi.org/10.1016/j.ocemod.2017.11.008, 2018.

Wiggins, S.: The dynamical systems approach to Lagrangian transport in oceanic flows, Annu. Rev. Fluid Mech., 37, 295–328, https://doi.org/10.1146/annurev.fluid.37.061903.175815, 2005.